Materials Chemistry and Physics 138 (2013) 542–552

Contents lists available at SciVerse ScienceDirect

Materials Chemistry and Physics

journal homepage: www.elsevier.com/locate/matchemphys

Highly air stable branched octithiophene oligomer for organic field effect transistor and pH sensor applications

Hung-Chin Wu, Wen-Ya Lee, Chih-Jung Lin, Wen-Chang Chen*

Department of Chemical Engineering, National Taiwan University, Taipei 10617, Taiwan

HIGHLIGHTS

- Novel highly air-stable branched octithiophene oligomer **8T**.
- **8T** showed a highly crystalline structure with a field-effect mobility of 2.12 × 10^{-2} cm^2 V^{-1} s^{-1} and an on/off ratio of 5.1 × 10^6.
- **8T** sensor devices maintained the stable device performance under aqueous conditions.

GRAPHICAL ABSTRACT

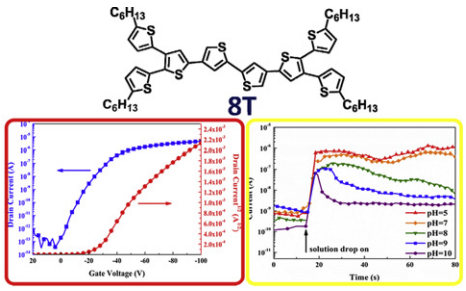

ARTICLE INFO

Article history:
Received 21 August 2012
Received in revised form
9 November 2012
Accepted 2 December 2012

Keywords:
Organic compounds
Crystal structure
Electrical properties
Thin films

ABSTRACT

We report the synthesis, morphology, and organic field effect transistor (OFET) characteristics of novel branched octithiophene oligomer: 5,5′′′′-dihexyl-3′,5′′′-bis(5-hexylthiophen-2-yl)-2,2′:5′,3″:5″,2‴:4‴,2‴′:4‴′,2‴″-sexithiophene (**8T**) prepared by the Stille coupling reaction. The effects of the surface modification and film thickness on the crystallinity, charge transport and sensing characteristics were explored systematically. **8T** exhibited two absorption peaks at 300 and 350 nm with an optical band gap of 2.88 eV. It showed a highly crystalline structure with a melting point at 65 °C and had a lamellar packing structure, confirmed by grazing incidence small-angle X-ray scattering (GISAXS). Among different vapor-deposition conditions, the **8T** based OFETs showed the field effect mobility up to 2.12 × 10^{-2} cm^2 V^{-1} s^{-1} and a high on/off ratio of 5.1 × 10^6 on the bare substrate. The relatively low-lying HOMO energy level (−5.53 eV) of **8T** led to the outstanding air stability of the OFET device. Also, the **8T** sensor devices maintained the stable device performance under aqueous conditions, and the current ratio between pH values of 5 and 10 could be above 3 orders of magnitude. The above results demonstrated that the air-stable **8T** could be as a promising candidate for high performance organic electronic devices.

1. Introduction

Recently, organic semiconductors have been highly developed for applications in organic electronics such as light-emitting diodes (OLEDs) [1,2], field effect transistors (OFETs) [3–20], photovoltaic cells (OPVCs) [20–30], and memory devices [31–35] due to their advantages of low cost, light weight and the capability to fabricate flexible electronic devices. In additional, OFETs have attracted considerable interest for the potential applications in e-paper [36–38], radio-frequency identification (RFID) tags [39,40], and chemical sensors [41–43].

Among the organic semiconductors reported for OFETs, regioregular poly(3-alkylthiophene)s, oligothiophenes, and fused aromatic compounds have shown remarkable performance [4,5,13]. α-Conjugated oligothiophenes (α-nT) were widely investigated p-type organic semiconductors [3,4,6]. Because their structural flexibility for tuning morphology and electrical properties, such as dihexyl-α-sexithiophene (DHα-6T) and dihexyl-α-octithiophene (DHα-8T) However, the stability of α-nT materials was insufficient

* Corresponding author. Tel.: +886 2 23628398; fax: +886 2 23623040.
E-mail address: chenwc@ntu.edu.tw (W.-C. Chen).

0254-0584/$ – see front matter © 2012 Elsevier B.V. All rights reserved.
http://dx.doi.org/10.1016/j.matchemphys.2012.12.017

for the practical electronic device applications, because of the relatively high highest occupied molecular orbital (HOMO) energy level, leading to poor air stability [4,8]. Therefore, development of thiophene oligomers with a low HOMO level and highly crystalline structure may solve the air stability problem and have high carrier mobility.

Dendritic and hyperbranched oligothiophenes exhibited the relatively low-lying HOMO energy levels in comparison with linear oligothiophenes and thus improved air stability [19–22]. The HOMO energy level of various branched oligothiophene derivatives were about −5.20 eV (oligothiophene-based swivel-cruciforms) [19], −5.20 eV (star-shaped oligothiophene) [44], and −5.26 to −5.57 eV (X-shaped oligothiophene) [21–23], respectively. These values are lower than linear oligothiophenes (−5.00 eV) [15]. Thus, branched oligothiophenes may provide extended delocalized π-electrons for enhancing charge transport. For the OFET characteristics, the best performance of branched oligothiophenes is 0.012 $cm^2 V^{-1} s^{-1}$ [19], indicating their charge transport ability is comparable with that of linear oligothiophenes. On the other hand, the OFET devices performance could be further improved by optimizing the surface structure, such as the grain size, crystallinity, and hydrophobic/hydrophilic characteristics [13,45].

In this work, we report the synthesis, morphology, properties, and OFET device characteristics of new branched octithiophene oligomer: 5,5‴″-dihexyl-3′,5‴″-bis(5-hexylthiophen-2-yl)-2,2′:5′,3″:5″,2‴:4‴,2‴″:4‴″,2‴‴-sexithiophene (**8T**) synthesized via the Stille coupling reaction (Scheme 1). The morphology, thermal, optical, and electrochemical properties of **8T** were studied. The charge transport ability of **8T** was characterized by using the top-contact OFETs. Our study revealed that the newly prepared **8T** had the characteristics of high OFET mobility, air stability and pH sensing characteristics.

2. Experimental section

2.1. Materials

2,3-dibromothiophene, trimethyltin chloride and tetrakis (triphenyl-phosphine) palladium(0) were purchased from Aldrich (Missouri, USA), Alfa Aesar (Massachusetts, USA), and TCI (Tokyo, Japan), and used without further purification. Common organic solvents and ultra-anhydrous solvents, such as acetonitrile, tetrahydrofuran, and chloroform, were purchased from Aldrich (Missouri, USA) and used as received. Octadecyltrichlorosilane (95%) (ODTS) was purchased from Acros (Geel, Belgium). 2-Trimethylstannyl-5-hexylthiophene (**1**) and 4,4′-dibromo-2,2′-bithiophene (**4**) were synthesized according to our previous work [20,30].

2.2. Monomer synthesis

5,5″-dihexyl-2,2′:3′,2″-terthiophene (**2**). A solution of 2-trime thylstannyl-5-hexylthiophene (**1**, 6.5 g, 20 mmol), 2,3-dibromothiophene (1.9 g, 8 mmol), and $Pd(PPh_3)_4$ (0.2 g, 0.17 mmol) in DMF (20 mL) and toluene (80 mL) was mixed in a one-neck flask. After three freeze–thaw cycles, the mixtures was heated up to 110 °C for 24 h under nitrogen purging. After cooling to room temperature, water was added and then the aqueous phase was extracted with hexane. The organic extract was dried over $MgSO_4$ to remove water, and the solvent was evaporated under vacuum. The crude product was purified by flash column using hexane as eluent to give **2** (1.3 g, 40%) as a chartreuse oil. ^{1}H NMR (400 MHz, CD_2Cl_2), δ (ppm): 7.24 (d, 1H), 7.12 (d, 1H), 6.92 (d, 1H), 6.86 (d, 1H), 6.70 (m, 1H), 6.67 (m, 1H), 2.78 (m, 4H), 1.61–1.67 (m, 4H), 1.30–1.38 (m, 12H), 0.87–0.90 (m, 6H).

(5,5″-dihexyl-[2,2′:3′,2″-terthiophen]-5′-yl)trimethylstannane (**3**). n-BuLi (2.5 M in hexanes, 8.8 mL, 22 mmol) was added dropwise over 15 min to a solution of 5,5″-dihexyl-2,2′:3′,2″-terthiophene (**2**, 7.6 g, 18 mmol) in anhydrous THF at −78 °C under nitrogen. The reaction mixture was maintained with the temperature below −10 °C. After the mixture was stirred for 2 h, trimethyltin chloride (5.1 g, 25 mmol) was added in one portion, and then the cooling bath was removed. After the solution warmed to room temperature, the solution stirred at room temperature overnight and then Na_2CO_3 solution was added. In the following, the aqueous phase was extracted with ether twice. The organic extract was dried over $MgSO_4$ to remove water and concentrated to obtain **3** (10 g, 94%) as yellow oil. ^{1}H NMR (400 MHz, CD_2Cl_2), δ (ppm): 7.15 (s, 1H), 6.88 (d, 1H), 6.85 (d, 1H), 6.67 (m, 2H), 2.78 (m, 4H), 1.60–1.67 (m, 4H), 1.25–1.39 (m, 12H), 0.83–0.90 (m, 6H), 0.37 (t, 9H).

5,5‴″-dihexyl-3′,5‴″-bis(5-hexylthiophen-2-yl)-2,2′:5′,3″:5″,2‴:4‴,2‴″:4‴″,2‴‴-sexithiophene (**5**, **8T**). A solution of (5,5″-dihexyl-

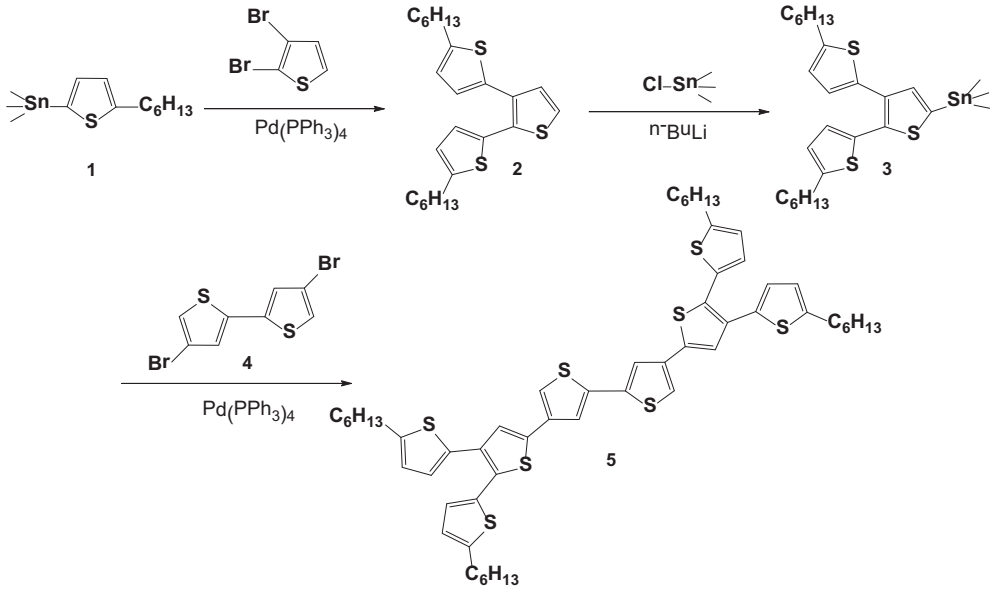

Scheme 1. Synthetic route of 5,5‴″-dihexyl-3′,5‴″-bis(5-hexylthiophen-2-yl)-2,2′:5′,3″:5″,2‴:4‴,2‴″:4‴″,2‴‴-sexithiophene (**5**) (**8T**).

[2,2′:3′,2″-terthiophen]-5′-yl)-trimethylstannane (**3**, 10.5 g, 18 mmol), 4,4′-dibromo-2,2′-bithiophene (**4**, 2.3 g, 7 mmol), and $Pd(PPh_3)_4$ (0.2 g, 0.17 mmol) in DMF (50 mL) were mixed in a one-neck flask. After three freeze–thaw cycles, the mixtures were heated up to 100 °C for 24 h under nitrogen atmosphere. After cooling to room temperature, water was added and then the aqueous phase was extracted with hexane. The organic extract was dried over $MgSO_4$ to remove water, and the solvent was evaporated under vacuum. The crude product was recrystallized by hexane to give **5** (4.6 g, 64%) as a yellow solid. ^{1}H NMR (400 MHz, CD_2Cl_2), δ (ppm): 7.42 (d, 2H), 7.32 (d, 2H), 7.24 (s, 2H), 6.95 (d, 2H), 6.90 (d, 2H), 6.68 (m, 4H), 2.78 (m, 8H), 1.62–1.66 (m, 8H), 1.27–1.37 (m, 24H), 0.86–0.89 (m, 12H). Anal. Calcd. for [$C_{56}H_{66}S_8$]: C, 67.55; H, 6.68; S, 25.76. Found: C, 67.43; H, 6.84; S, 25.93.

2.3. Characterization

^{1}H NMR spectra were recorded by Bruker Avance DRX-400 MHz spectrometer. Thermogravimetric analysis (TGA) and differential scanning calorimetry (DSC) measurements were performed under a nitrogen atmosphere at a heating rate of 10 and 5 °C min^{-1} using the TA instruments Q-50 and Q-100, respectively.

Atomic force microscopy (AFM) measurements were obtained with a NanoScope IIIa AFM (Digital Instruments, Santa Barbara, CA) at room temperature. Commercial silicon cantilevers with typical spring constants of 21–78 N m^{-1} were used to operate the AFM in tapping mode. Images were taken continuously with the scan rate of 1.0 Hz. Grazing incidence small-angle X-ray scattering (GISAXS) was conducted on beamline BL23A1 in the National Synchrotron Radiation Research Center (NSRRC), Taiwan. A monochromatic beam of λ = 1.240 Å was used. The scattering patterns were collected on a Mar-CCD with a diameter of 165 mm [46]. X-ray diffraction (XRD) was performed by X'Pert PRO X-ray diffractometer using Cu-Kα radiation (λ = 1.5418 Å) with a scan range typically of 2–35°, 0.2° per step. The thickness of polymer film was measured with a Microfigure Measuring Instrument (Surfcorder ET3000, Kosaka Laboratory Ltd.).

UV–vis absorption spectrum was recorded on a Hitachi U-4100 spectrophotometer. For the thin film spectra, **8T** was first dissolved in chloroform (20 mg ml^{-1}), followed by filtering through a 0.45 μm pore size PTFE membrane syringe filter, and then spin-coated at a speed rate of 1000 rpm for 60 s onto quartz substrate. Cyclic voltammetry (CV) was performed with the use of a three-electrode cell in which ITO (**8T** films area were about 0.5 × 0.7 cm^2) was used as a working electrode. A platinum wire was used as an auxiliary electrode. All cell potentials were taken with the use of a Ag/AgCl, KCl (sat.) reference electrode. The electrochemical properties of the **8T** films were detected under 0.1 M anhydrous acetonitrile solution containing tetrabutylammonium perchlorate (TBAP) as electrolyte.

The surface energy of the substrates and **8T** thin film was calculated by measuring the contact angles of the two liquids, water and diiodomethane, respectively. The surface energies of these surfaces were obtained by the following equation [18]:

$$(1+\cos\theta)\gamma_{IV} = 2\left(\gamma_S^D\right)^{1/2}\left(\gamma_{IV}^D\right)^{1/2} + 2\left(\gamma_S^P\right)^{1/2}\left(\gamma_{IV}^P\right)^{1/2} \quad (1)$$

where γ_S^D and γ_S^P are the dispersion and polar components of the surface energy, respectively, and the liquid vapor interface surface energy (γ_{IV}), the dispersion component (γ_{IV}^D) and the polar component (γ_{IV}^P) values were 72.2, 22.0 and 50.2 mJ m^{-2} for water and 50.8, 48.5 and 2.3 mJ m^{-2} for diiodomethane. Finally, the surface energy of the substrate layer (γ_S) was calculated as the following [18]:

$$\gamma_S = \gamma_S^D + \gamma_S^P \quad (2)$$

2.4. Fabrication and characterization of field effect transistors

Highly doped n-type Si (100) wafers were used as substrates. A 300 nm SiO_2 layer (capacitance per unit area C_i = 10 nF cm^{-2}) as a gate dielectric was thermally grown onto the Si substrates. These wafers were cleaned in piranha solution, a 7:3 mixture of H_2SO_4 and H_2O_2, rinsed with deionized water, and then dried by N_2. Octadecyltrichlorosilane (ODTS)-treated surface on SiO_2 were prepared by the following procedures: the cleaned substrates were immersed into a 10 mM solution of ODTS in anhydrous toluene at room temperature for overnight. Then, the substrate was rinsed with toluene, acetone, isopropyl alcohol, and dried with a steam of nitrogen. OFET device was deposited by thermal evaporation at a rate of 0.3–0.5 Å s^{-1} under a pressure of 9 × 10^{-7} Torr on ODTS-treated or bare substrates. The substrate temperature was controlled by a heating source during deposition, and **8T** was deposited at the range of 25–80 °C with different film thickness. The top-contact source and drain electrodes were defined by 100 nm-thick gold through a regular shadow mask, and the channel length (L) and width (W) were 50 and 1000 μm, respectively. OFETs transfer and output characteristics were recorded in a N_2-filled glove box or in ambient by using a Keithley 4200 semiconductor parametric analyzer. In the case of OFET for pH sensing, a 50 nm layer of silicon monoxide was thermally evaporated on the electrodes prevent the electrode from the damage of water.

3. Results and discussion

3.1. Structure characterization

The chemical structure of **8T** was confirmed by ^{1}H NMR in CD_2Cl_2, as shown in Fig. 1. The resonance peaks, at 7.42 (peak a), 7.32 (peak b), 7.24 (peak c), 6.95 (peak d), 6.90 (peak e), and 6.68 (peak f) ppm are assigned to the protons on the thiophene rings. On the other hand, the proton peaks at 2.78 (peak g), 1.62–1.66 (peak h), 1.27–1.37 (peak i), and 0.86–0.89 (peak j) ppm are attributed to the hexyl group in the **8T**. The numbers of aliphatic and aromatic protons were estimated from the integration value of peaks, and consistent with the proposed chemical structure. The ^{1}H NMR spectrum of the precursor, 5,5″-dihexyl-2,2′:3′,2″-terthiophene (**2**), is also consistent with the proposed chemical structure (Fig. S1 of the Supplementary information). Moreover, the elemental analysis of **8T** is in a good agreement with the theoretical content. The above results indicate the successful preparation of **8T**.

3.2. Thermal properties

The thermal decomposition temperature (T_d, 95 wt% residue) of **8T** estimated from thermogravimetric analysis (Fig. S2 of the Supplementary information) is 388 °C, indicating its good thermal stability for electronic devices. The DSC curve of **8T** shown in Fig. 2 has a phase transition temperature at 52 °C (T_c) followed by an isotropic transition at 65 °C (T_m). It implies that the intermolecular packing of **8T** can be manipulated by controlling thermal deposition temperatures.

3.3. Optical and electrochemical properties

The UV–vis absorption spectra of **8T** in dilute chloroform and thin films are shown in Fig. 3(a). **8T** has two absorption peak maximum wavelengths (λ_{max}): the one at longer wavelength around 325–380 nm (λ_{max} at ca. 350 nm) is corresponding to the π–π^* transition, while the shorter wavelength around 250–320 nm (λ_{max} at ca. 300 nm) comes from the electronic transition of the individual thiophene moiety [7]. The optical band gap (E_g^{opt})

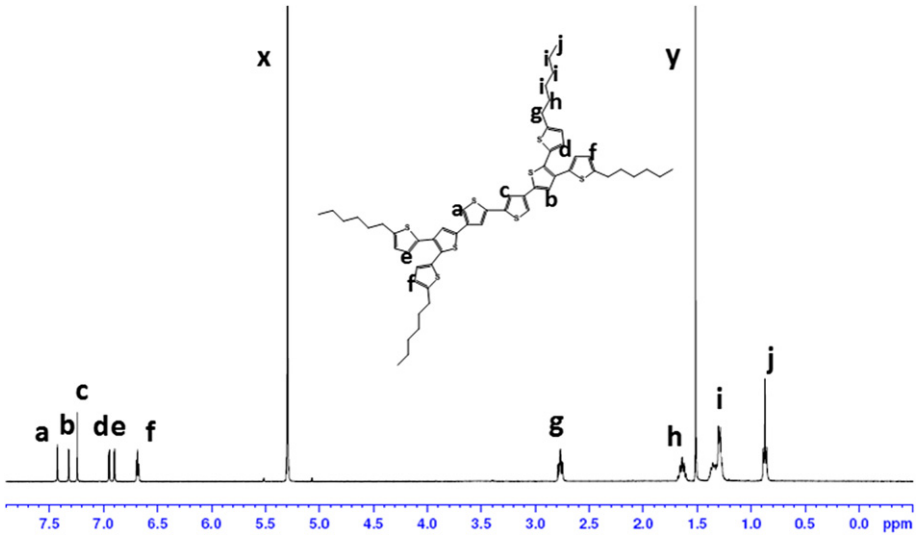

Fig. 1. ^{1}H NMR spectrum of **8T** in CD_2Cl_2. (x: CD_2Cl_2, y: H_2O).

of **8T** estimated from the long-wavelength absorption edge is 2.88 eV.

Fig. 3(b) shows the cyclic voltammetry (CV) curves of **8T** thin films in acetonitrile at a potential scan rate of 100 mV s^{-1}. The HOMO energy level of **8T** was estimated from onset oxidation potentials (E^{ox}_{onset}), based on the following equations: HOMO $= -[E^{ox}_{onset} - E^{ferrocene}_{1/2} + 4.8]$ eV, where the potentials are referred to an Ag/AgCl reference electrode. The obtained HOMO energy level of **8T** was −5.53 eV, which was relatively low-lying in comparison with those of the reported branched oligothiophene derivatives [19,21–23,44] and suggested its good air stability.

3.4. Atomic force microscopy (AFM) characteristics

The surface structures of **8T** vapor-deposited films with different thickness of 25–100 nm, annealing temperatures of 25–80 °C, and surface modification (ODTS-treated or bare substrate) were investigated by atomic force microscopy (AFM). The AFM images of all **8T** thin films are shown in Figs. 4 and 5, Figs. S3 and S4 (Supplementary information). Generally, all the thin films show well-connected crystallites similar to common oligothiophenes [7,47]. However, as the substrate temperatures raised above 65 °C, the grain

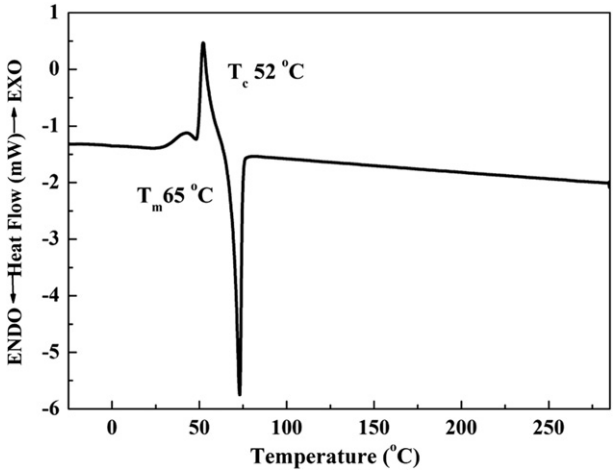

Fig. 2. DSC curve of **8T** at the heating rate of 5 °C min^{-1} under a nitrogen atmosphere.

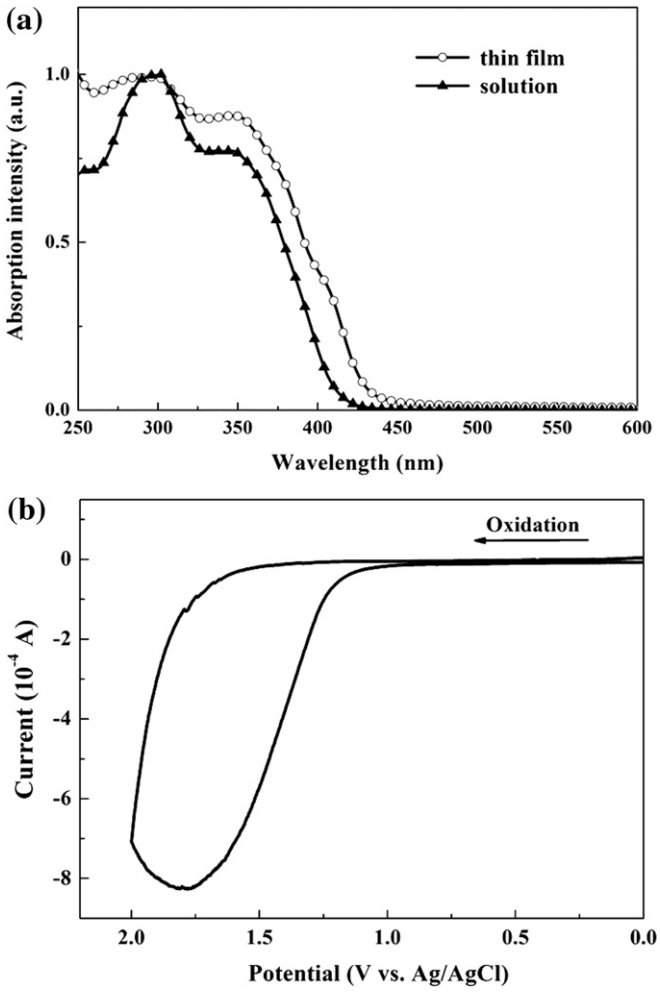

Fig. 3. (a) Optical absorption spectra of **8T** in dilute $CHCl_3$ solution and thin film on a quartz plate. (b) Cyclic voltammograms of **8T** thin film in an acetonitrile solution of 0.1 M TBAP at a scan rate of 100 mV s^{-1}.

boundaries are melted together and many deep gaps are formed with large surface roughness, particularly on the ODTS-treated substrate. For 50 nm-thick thin films, both on the bare and the ODTS-treated substrates, **8T** is consisted of well-connected grains as the film is deposited at room temperature. When the deposition temperature is elevated to 60 °C (Fig. 4), the surface structure has a significant change that the grains become larger. On the other hand, when the deposition temperature is raised higher than the melting point of **8T** (65 °C), the grain size is increased to micrometer scale, and many deep gaps between grains are formed. Note that the surface roughness of **8T** film on the bare substrate is smaller comparing to the ODTS-treated substrate probably owing to the better adhesion on the bare substrates. The surface energies of the ODTS-treated substrate, the bare substrate, and **8T** are 26.9, 54.1, and 45.5 mJ m^{-2}, estimated from the contact angles of water (91.2°) and diiodomethane (29.1°) using the method reported in the literature [18]. The larger surface energy mismatch between **8T** and the ODTS-treated substrates probably leads to the poorer adhesion for **8T** on the ODTS-treated surface. Furthermore, as the deposition temperature increase, **8T** has a larger kinetic energy to form large aggregates (Fig. 4) on the substrate surface and become more disordered. Therefore, **8T** cannot form a uniform crystalline film on the ODTS-treated substrates as the deposition temperature of above 65 °C.

In addition, the effect of film thickness on the surface structure is shown in Fig. 5. As the substrate temperature is controlled at 60 °C, 25 nm-thick film seems too thin to grow the regular grains and the roughness is slightly large. When the film thickness is increased above 50 nm, well-connected grains are formed, and the surface roughness is generally smaller than 3.5 nm. However, if the film thickness is raised to 100 nm, the roughness increases again as shown in Fig. S4 of the Supplementary information.

3.5. X-ray diffraction (XRD) characteristics

The grazing incidence small-angle X-ray scattering (GISAXS) patterns of all **8T** thin films with different processing conditions are shown in Figs. 6 and 7, Figs. S5 and S6 (Supplementary information). Generally, **8T** is a highly crystalline thin film with different processing condition. From the 2D GISAXS pattern, strong diffraction signals are observed in q_z direction but not in the q_y direction. Moreover, a strong peak at 3° (d-spacing = 14.73 $Å^{-1}$) of the X-ray diffractogram is observed in Fig. 6(e). The above result indicates that **8T** has a lamellar packing structure in q_z direction on the substrate. Interestingly, in the q_z direction of the GISAXS pattern, around the main diffraction peak, the present of multiple Bragg reflections and Laue oscillations demonstrates that **8T** thin films possess long-range ordering in the thin film [17,48].

The **8T** film (thickness: 50 nm) on the bare substrate with different deposition temperatures all exhibit a high crystallinity, as shown in Fig. 6, and Fig. S5 (Supplementary information). From the multiple diffraction peaks in Fig. 6(b), the film thickness is

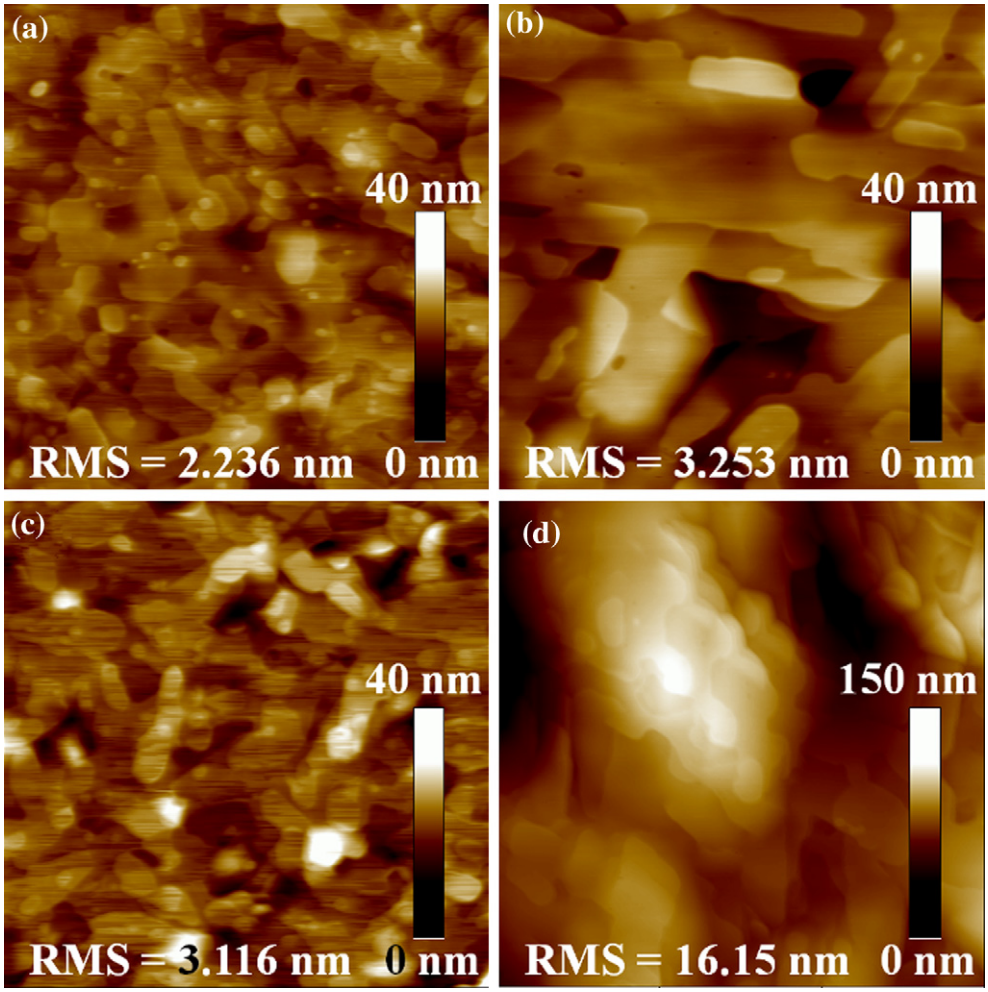

Fig. 4. Tapping mode AFM images of **8T** films (thickness: 50 nm) using different vapor-deposition temperatures: (a) 60 °C, and (b) 70 °C on the bare substrates; (c) 60 °C, and (d) 70 °C on the ODTS-treated substrates. All images are 3 μm × 3 μm in sizes.

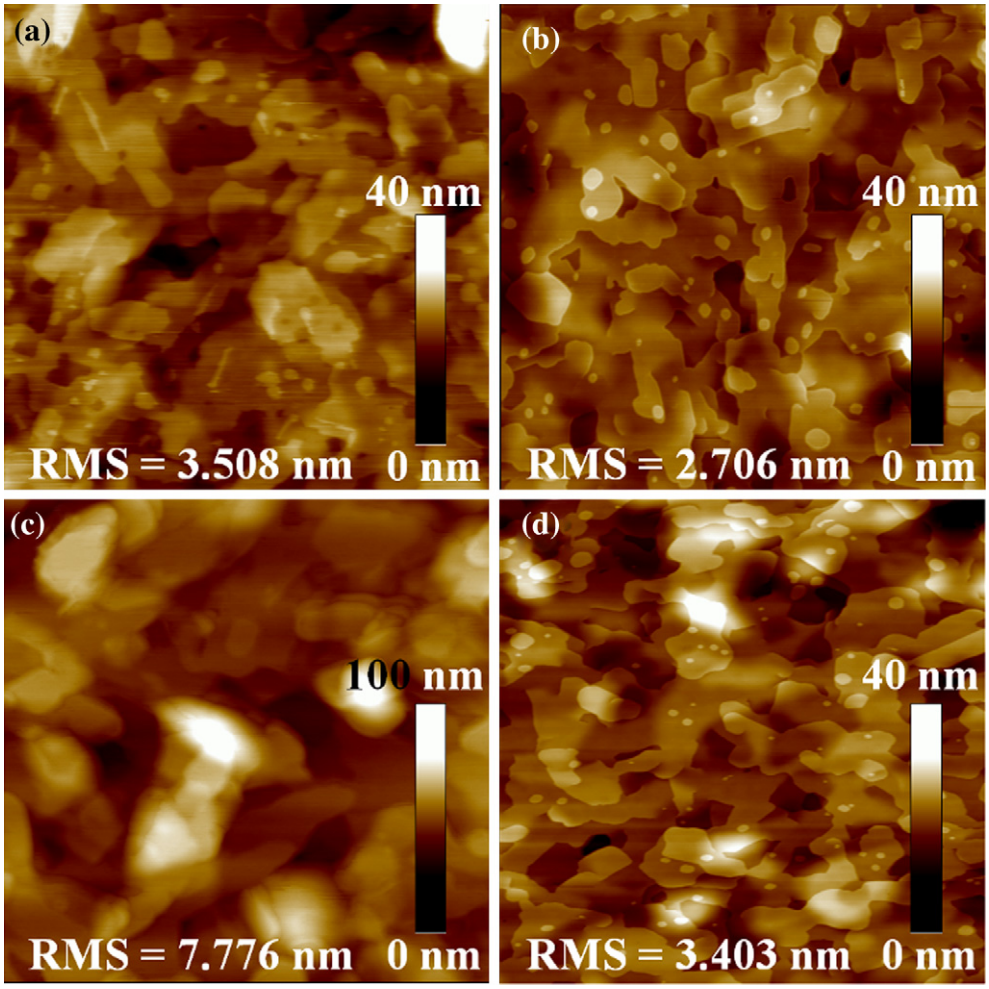

Fig. 5. Tapping mode AFM images of **8T** films vapor-deposited at 60 °C with different thicknesses: (a) 25 nm and (b) 75 nm on the bare substrates; (c) 25 nm and (d) 75 nm on the ODTS-treated substrates. All images are 3 μm × 3 μm in sizes.

estimated to be 52 nm and consistent with the result of microfigure measurement. However, from the multiple diffraction signals in Fig. 6, the crystallinity of **8T** thin film decreases on the ODTS-treated substrate as the deposition temperature is increased. Especially when the temperature is heated above the melting temperature of **8T** (65 °C), the multiple diffraction patterns are vanished and only the arc pattern is observed.

Fig. 7 and Fig. S6 (Supplementary information) show the GISAXS patterns of **8T** on the bare or the ODTS-treated substrates with different film thickness with the vapor-deposition temperature of 60 °C. **8T** films on the bare substrates all show high crystallinity at different film thickness. Compared to the bare substrates, **8T** films on the ODTS-treated substrates exhibit less crystallinity, probably due to poor adhesion between **8T** and substrate surface [18].

The GISAXS and XRD results indicate that **8T** film on the bare substrate have a higher crystallinity than that on the ODTS-treated substrate. From the X-ray diffractogram (Fig. 6(e)), the full widths at half-maximum on the bare and ODTS-treated substrates are approximately 0.052 and 0.064, respectively. It suggests that **8T** has a higher degree of texturing and ordering on the bare substrate than that on the ODTS-treated substrates due to the better adhesion [17]. When **8T** deposited on the ODTS-treated substrates at a high temperature, the relative low surface energy of the ODTS-treated substrate facilitates the movement of **8T** on the substrate surfaces to reduce the crystallinity [18].

3.6. Organic field-effect transistor (OFET) characteristics

All OFET devices were fabricated by employing top-contact device geometries for reducing contact resistance [9]. The OFET characteristics of **8T** using different deposition temperature (25–80 °C) and film thickness (25–100 nm) are summarized in Tables 1 and 2. The saturation-regime mobility was calculated from the slope of the plot of drain-source current $(I_{DS})^{1/2}$ as a function of the gate voltage (V_g) [49]. The p-type output characteristics of **8T** with different processing conditions are shown in Fig. 8 and Fig. S7 (Supplementary information), which exhibit well-defined linear and saturation regions with a good current modulation. Moreover, the transfer characteristics are represented in Fig. 8, Figs. S8 and S9 (Supplementary information). On the bare substrates, the maximum mobilities of the **8T** OFETs using the 50-nm-thick films using different deposition temperature are 7.71×10^{-3} (25 °C), 1.59×10^{-2} (50 °C), 2.12×10^{-2} (60 °C), 1.89×10^{-2} (70 °C), and 1.52×10^{-2} (80 °C) $cm^2\ V^{-1}\ s^{-1}$, respectively, while those on the ODTS-treated substrate are 3.63×10^{-3} (25 °C), 6.19×10^{-3} (50 °C), 1.34×10^{-2} (60 °C), 5.65×10^{-4} (70 °C), and 5.11×10^{-4} (80 °C) $cm^2\ V^{-1}\ s^{-1}$, respectively. The on/off ratios for all devices on the bare and the ODTS-treated substrates range from 10^5 to 10^6. In additional, **8T**-based OFETs show a small hysteresis around 10 V under the dual-sweep *I–V* scan (Fig. S10 in Supplementary information). This hysteresis may be attributed to

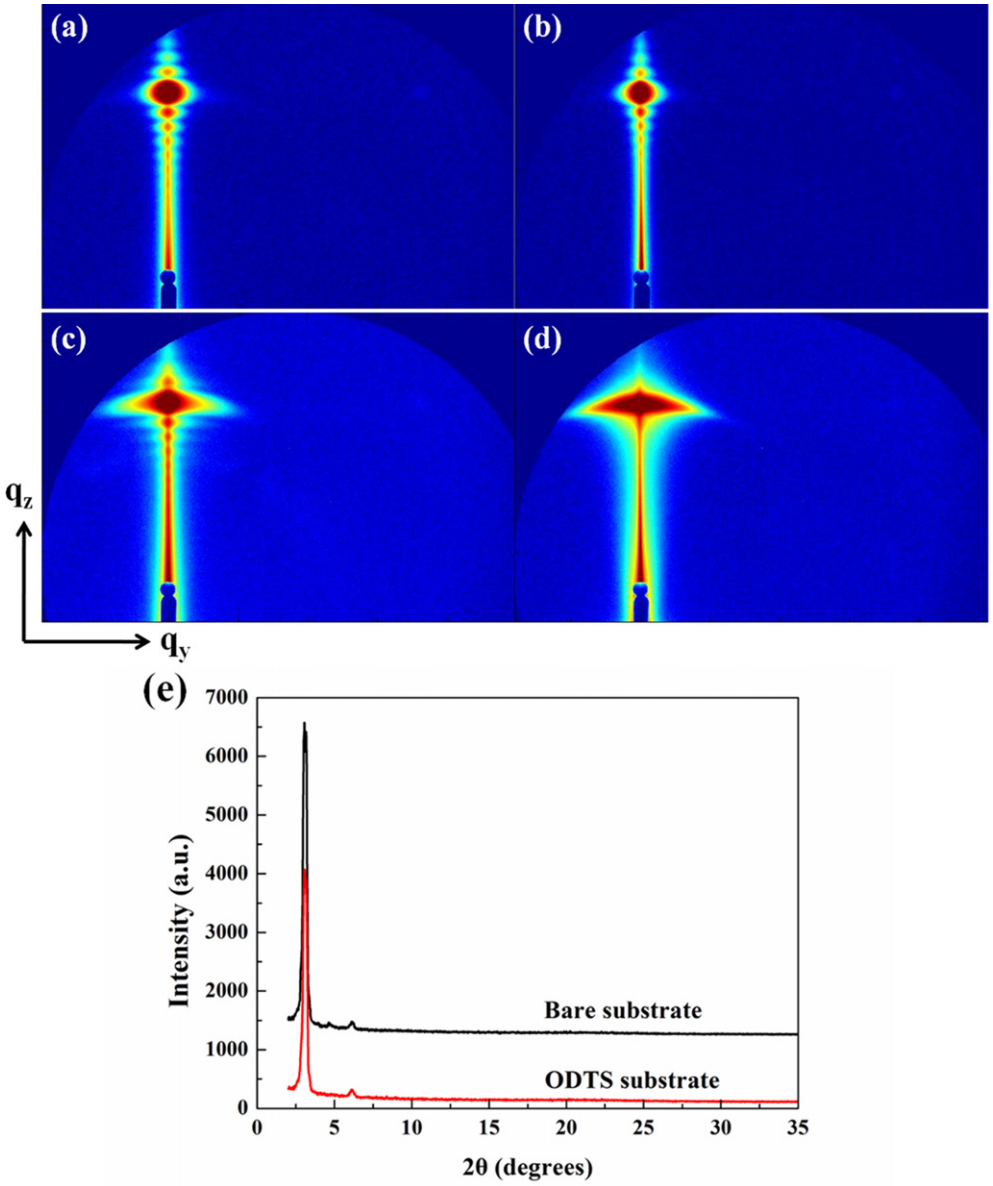

Fig. 6. GISAXS patterns of **8T** film with the thickness of 50 nm using different vapor-deposition temperatures: (a) 60 °C, and (b) 70 °C on the bare substrates; (c) 60 °C, and (d) 70 °C on the ODTS-treated substrates. The range of q_y is from −0.1 to 0.25 Å^{-1}, q_z is from 0 to 0.23 Å^{-1}. (e) X-ray diffractograms of **8T** film (thickness: 50 nm) vapor-deposited at 60 °C on the bare and ODTS-treated substrate.

the hydroxyl group on the bare substrate [50]. For the **8T** OFET devices on the bare and ODTS-treated substrates, the hole mobilities generally increase with the elevated deposition temperature as the deposition temperature lower than 70 °C [45,51]. The best performance is observed at substrates temperature of 60 °C, due to the less grain boundaries and larger crystallite grain sizes. The lower mobility of **8T** film on the ODTS-treated substrates is probably due to the poor adhesion [18], reducing the interconnection between grains. Consequently, the hole mobilities decrease due to the deep grain boundaries [45,50] when the deposition temperature increase over 70 °C.

To further investigate the relationship between mobilities and channel thickness, the deposition temperature is controlled at 60 °C. The maximum mobilities of the OFETs fabricated with different thickness on the bare substrates are 1.27×10^{-2} (25 nm), 2.12×10^{-2} (50 nm), 2.12×10^{-2} (75 nm), and 5.16×10^{-3} (100 nm) cm^2 V^{-1} s^{-1}, respectively, while those on the ODTS-treated substrates are 1.32×10^{-2} (25 nm), 1.34×10^{-2} (50 nm), 1.15×10^{-2} (75 nm), and 9.43×10^{-4} (100 nm) cm^2 V^{-1} s^{-1}, respectively. The on/off ratios for all devices on the bare and the ODTS-treated substrates are up to 10^6. From the AFM images, the connection between grain crystals is enhanced with the increase of the film thickness on the bare substrates, leading to better charge carrier transporting. On the contrary, OFETs with thinner thickness, a shorter charge carrier transport path from the interface of **8T**/SiO_2 to drain electrodes results in better hole-transporting [52]. Therefore, an optimum thickness to have the highest mobility is 75 nm because 100 nm film thickness has a large resistance. The threshold voltages (V_t) of **8T** devices are quite high. This is due to its relatively low-lying HOMO energy level of −5.53 eV, leading to a large hole-injection barrier between **8T** and Au electrodes (−5.1 eV) [10]. The highest mobility of **8T** OFET device in this study is

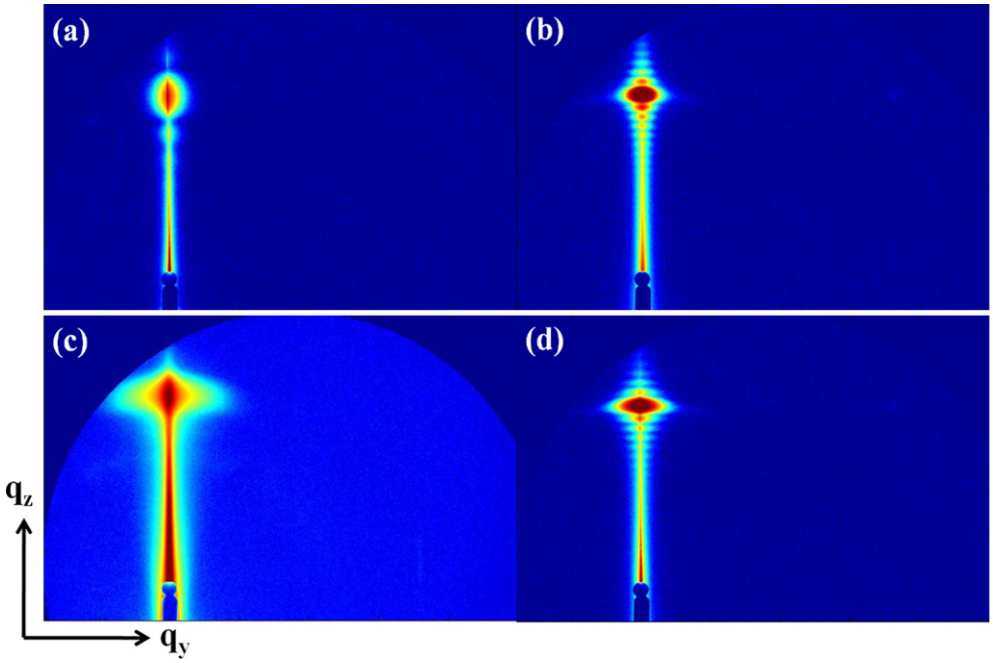

Fig. 7. GISAXS patterns of **8T** vapor-deposited at 60 °C with different film thicknesses: (a) 25 nm and (b) 75 nm on the bare substrates; (c) 25 nm and (d) 75 nm on the ODTS-treated substrates. The range of q_y is from −0.1 to 0.25 Å^{-1}, q_z is from 0 to 0.23 Å^{-1}.

2.12×10^{-2} cm^2 V^{-1} s^{-1} on the bare substrate, which is among the best mobilities reported in the branched oligothiophenes [19,23,24,44].

3.7. Air stability of the OFET device

The air stability of the devices is monitored by measuring hole mobility and on/off ratio as a function of time, as shown in Fig. 9. **8T** OFET exhibits great air stability on the bare and the ODTS-treated substrates, and the corresponding mobility decreased slightly from 7.36×10^{-3} to 3.56×10^{-3} and from 1.10×10^{-2} to 6.31×10^{-3} cm^{-2} V^{-1} s^{-1}, respectively, after exposure to air for about one month. The high crystallinity and the relatively low-lying HOMO energy level (−5.53 eV) could resist the intrusion of oxygen and moisture, showing excellent air-stable performance and a large on/off current ratio of 10^6 in air. Intriguingly, the **8T** OFET on the ODTS-treated substrate exhibited higher ambient stability than that on the bare substrate. It is attributed to the fact that the ODTS-treated surface possesses a hydrophobic long alkyl chain, preventing the influence of oxygen and moisture, thus leading to better air stability [53,54].

3.8. pH sensor characteristics

For the case of OFET for sensor applications, it is important that the active layer material possesses a low-lying HOMO energy level can eschew the doping of moisture and oxygen for enhancing the operating stability. Furthermore, **8T** with a highly-crystalline hydrophobic surface provides a good charge transporting ability and kinetically reduce the penetration of water. Therefore, **8T** may have stable OFET performance under aqueous conditions for sensory applications.

Sensory applications under aqueous conditions are characterized using the **8T** OFET on the bare substrate with the optimized condition of substrate temperature at 60 °C and 75 nm thickness. The top-contact gold electrodes were encapsulated by 50-nm-thick silicon monoxide. The applied source–drain voltage bias is controlled below −30 V to reduce the influence of degradation and delamination in aqueous phase. In ambient condition, we observe stable device performance with the source–drain voltage bias is controlled at −30 V, as shown by the black curve in Fig. 10(a). After dropping water onto the channel, a positive shift is observed in threshold voltage and an increase in the on and off currents due to hydronium (H_3O^+) doping, as shown by the blue curve (in the web

Table 1
OFET device characteristics of **8T** with the film thickness of 50 nm at different substrate temperature (T_s).

T_s (°C)	Substrate surface	Mobility^{max} (cm^2 V^{-1} s^{-1})	Mobility^{avg} (cm^2 V^{-1} s^{-1})	On/off^{avg}	V_t^{avg} (V)
25	Bare	7.71×10^{-3}	$(6.31 \pm 1.03) \times 10^{-3}$	4.6×10^6	-22 ± 0.3
	ODTS	3.63×10^{-3}	$(2.26 \pm 0.68) \times 10^{-3}$	3.6×10^5	-32 ± 12
50	Bare	1.59×10^{-2}	$(1.17 \pm 0.14) \times 10^{-2}$	5.6×10^6	-30 ± 4
	ODTS	6.19×10^{-3}	$(3.06 \pm 1.27) \times 10^{-3}$	1.1×10^6	-21 ± 6
60	Bare	2.12×10^{-2}	$(1.32 \pm 0.39) \times 10^{-2}$	5.1×10^6	-35 ± 6
	ODTS	1.34×10^{-2}	$(9.58 \pm 0.37) \times 10^{-3}$	1.2×10^6	-24 ± 3
70	Bare	1.89×10^{-2}	$(1.21 \pm 0.20) \times 10^{-2}$	5.1×10^6	-25 ± 9
	ODTS	5.65×10^{-4}	$(3.42 \pm 1.07) \times 10^{-4}$	1.0×10^5	-17 ± 2
80	Bare	1.52×10^{-2}	$(1.12 \pm 0.18) \times 10^{-2}$	4.3×10^6	-26 ± 4
	ODTS	5.11×10^{-4}	$(2.94 \pm 0.24) \times 10^{-4}$	3.5×10^5	-19 ± 2

Table 2
OFET device characteristics of **8T** are deposited at 60 °C with different film thickness.

Film thickness (nm)	Substrate surface	Mobility^{max} (cm^2 V^{-1} s^{-1})	Mobility^{avg} (cm^2 V^{-1} s^{-1})	On/off^{avg}	V_t^{avg} (V)
25	Bare	1.27×10^{-2}	$(6.65 \pm 1.56) \times 10^{-3}$	1.0×10^6	-26 ± 6
	ODTS	1.32×10^{-2}	$(1.04 \pm 0.15) \times 10^{-2}$	5.1×10^6	-44 ± 12
50	Bare	2.12×10^{-2}	$(1.32 \pm 0.39) \times 10^{-2}$	5.1×10^6	-35 ± 6
	ODTS	1.34×10^{-2}	$(9.58 \pm 0.37) \times 10^{-3}$	1.2×10^6	-24 ± 3
75	Bare	2.12×10^{-2}	$(1.28 \pm 0.16) \times 10^{-2}$	2.0×10^6	-30 ± 4
	ODTS	1.15×10^{-2}	$(8.86 \pm 1.63) \times 10^{-3}$	3.6×10^6	-48 ± 16
100	Bare	5.16×10^{-3}	$(3.50 \pm 0.96) \times 10^{-3}$	2.4×10^6	-33 ± 8
	ODTS	9.43×10^{-4}	$(4.63 \pm 1.50) \times 10^{-4}$	8.1×10^5	-28 ± 4

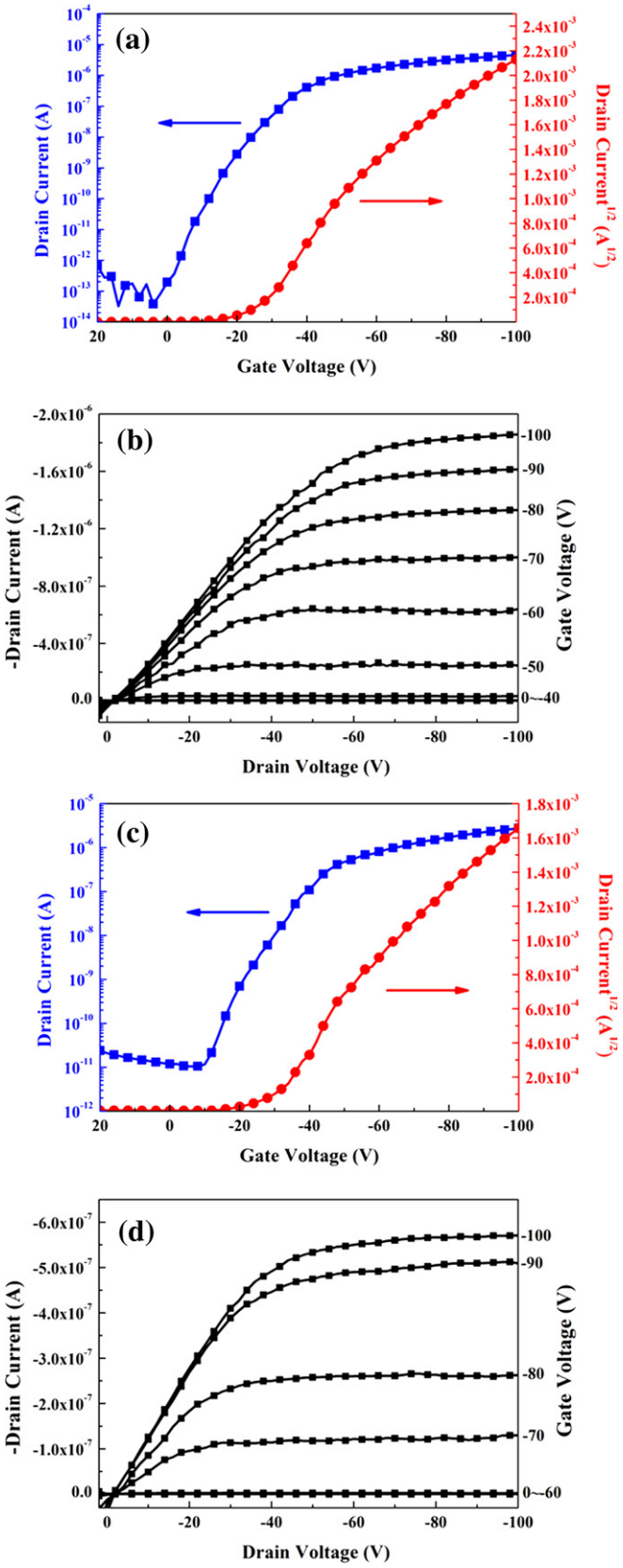

Fig. 8. P-type transfer characteristics of OFETs ($V_{ds} = -100$ V) using **8T** film (thickness: 50 nm) vapor-deposited at 60 °C on (a) the bare substrate, and (c) the ODTS-treated substrate; P-type output characteristics of OFETs using **8T** films on (b) the bare substrate, and (d) the ODTS-treated substrate.

version). In additional, transfer characteristics of pentacene-based OFETs in ambient and aqueous conditions are shown in Fig. S11 (Supplementary information). Pentacene-based devices cannot show typical transfer characteristics under aqueous condition owing to its poor environmental stability as well as high-lying HOMO level. The stability of materials acts a crucial role for the sensor applications. Therefore, the highly-stable **8T** is more suitable materials for sensory device, as compared to pentacene.

To understand how pH values affecting the electrical behavior of the OFET devices, the influence of pH solution on the drain current is evaluated. The increase in drain current is observed when the devices are operated under aqueous conditions. This phenomenon could be ascribed to exposure onto either hydronium (H_3O^+) or hydroxide ions (OH^-) [42]. Fig. 10(b) shows that the drain current increases with decreased pH values, i.e. an increase of the concentration of H_3O^+. We observed that the H_3O^+ concentration forthrightly affects the current. First, when the pH solutions are dropped on the channel, the drain current is changed immediately from a low current level (10^{-9} A) to a high current level (10^{-6}–10^{-7} A), and as pH increases, the drain current decreases. This variation of drain current may be due to the fact that the drain current combines the hole current from the semiconductor film and the ionic current from the pH solutions [42]. The well-defined grain boundaries of the **8T** films may also facilitate H_3O^+ to penetrate into the channel region, thus observe an increase of 3 orders of magnitude on the drain current.

Secondly, probably due to an increasing coulomb blockade for pH 5 and 7 solutions, the slower response of drain current is observed. This means the repulsion of H_3O^+ by positive charges already occupying the channel, and diminishing the rate of H_3O^+ diffusion into the channel. For the pH 9 and 10 solutions, the concentration gradient of H_3O^+ is away from the channel and the diffusion of ions is unobstructed, so the drain current response becomes faster [55,56]. In the pH values from 5 to 10, the **8T** devices can maintain stable device characteristics in aqueous solution, and the current ratio between pH 5 and 10 can be above 3 orders. These results indicate that **8T** sensor devices can have good sensitivity in the aqueous condition.

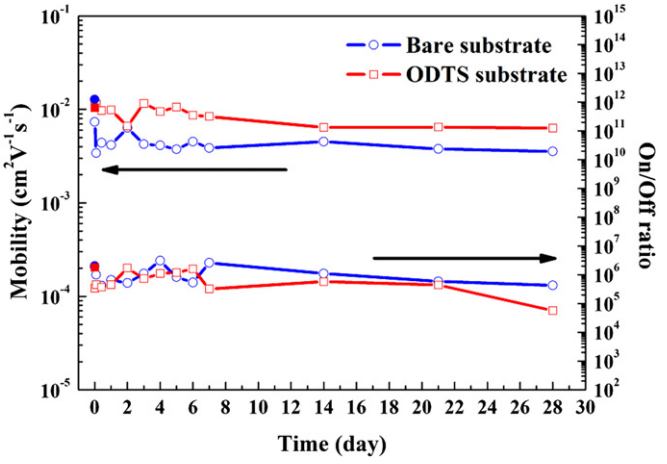

Fig. 9. Air-stability test on the OFET characteristics using **8T** thin films: (blue line, circle) – film thickness of 75 nm deposited at 60 °C on the bare substrate, and (red line, square): film thickness of 25 nm deposited at 60 °C on the ODTS-treated substrate. The solid symbols correspond to an electrical performance in a nitrogen glove box. Relative humidity ranges from 50 to 60% in air. (For interpretation of the references to color in this figure legend, the reader is referred to the web version of this article.)

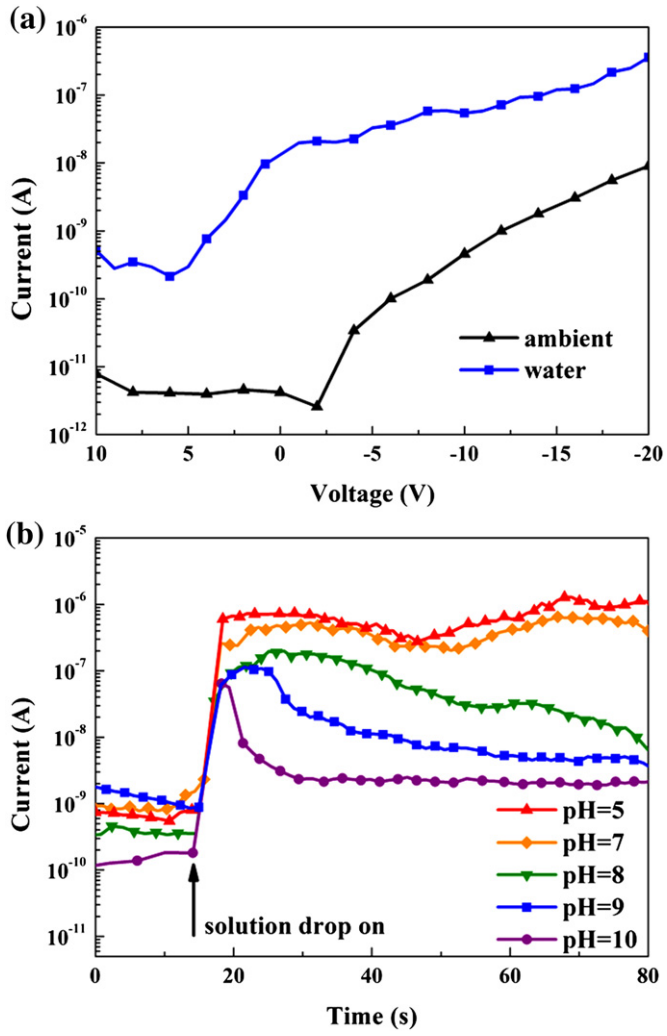

Fig. 10. (a) Transfer characteristics of **8T** film based OFETs operation under ambient and aqueous condition. (b) The drain current response of **8T** OFETs response to pH under aqueous condition.

4. Conclusions

We have successfully synthesized new branched octithiophene oligomer of **8T**, by palladium(0)-catalyzed Stille coupling reaction. **8T** had an optical band gap of 2.88 eV, and low HOMO energy level of −5.53 eV. The highest mobility (0.0212 $cm^2 V^{-1} s^{-1}$) of **8T** on bare substrate is due to the highly crystallinity, which was confirmed by AFM and GISAXS analysis. Moreover, the highly crystallinity and relatively low-lying HOMO energy level of **8T** reduce the chemical degradation and the intrusion of oxygen and moisture, showing great air-stable devices performance. With different pH solutions, the **8T** OFETs maintained stable device performance in aqueous solution, and the current ratio between pH 5 and 10 solutions was above 3 orders. The above results indicated that **8T** could enhance the air stability and charge-transport characteristics for OFET and sensory applications.

Acknowledgment

The financial support from National Science Council of Taiwan is highly appreciated. We acknowledge Dr. U-Ser Jeng and Dr. Chun-Jen Su of National Synchrotron Radiation Research Center (NSRRC), Taiwan for facilitating the GISAXS experiments.

Appendix A. Supplementary data

Supplementary data related to this article can be found at http://dx.doi.org/10.1016/j.matchemphys.2012.12.017.

References

[1] A.C. Grimsdale, K.L. Chan, R.E. Martin, P.G. Jokisz, A.B. Holmes, Chem. Rev. 109 (2009) 897–1091.
[2] W.C. Wu, C.L. Liu, W.C. Chen, Polymer 47 (2006) 527–538.
[3] A.R. Murphy, J.M.J. Frechet, P. Chang, J. Lee, V. Subramanian, J. Am. Chem. Soc. 126 (2004) 1596–1597.
[4] R. Hajlaoui, D. Fichou, G. Horowitz, B. Nessakh, M. Constant, F. Garnier, Adv. Mater. 9 (1997) 557–561.
[5] M. Mas-Torrent, C. Rovira, Chem. Rev. 111 (2011) 4833–4856.
[6] H.-S. Seo, Y. Zhang, Y.-S. Jang, J.-H. Choi, Appl. Phys. Lett. 92 (2008) 223310.
[7] H. Meng, J. Zheng, A.J. Lovinger, B.C. Wang, P.G. Van Patten, Z. Bao, Chem. Mater. 15 (2003) 1778–1787.
[8] J.H. Gao, R.J. Li, L.Q. Li, Q. Meng, H. Jiang, H.X. Li, W.P. Hu, Adv. Mater. 19 (2007) 3008–3011.
[9] A.R. Murphy, J.M.J. Frechet, Chem. Rev. 107 (2007) 1066–1096.
[10] K. Oikawa, H. Monobe, K. Nakayama, T. Kimoto, K. Tsuchiya, B. Heinrich, D. .Guillon, Y. Shimizu, M. Yokoyama, Adv. Mater. 19 (2007) 1864–1868.
[11] J.H. Oh, S.-L. Suraru, W.-Y. Lee, M. Koenemann, H.W. Hoeffken, C. Roeger, R. Schmidt, Y. Chung, W.-C. Chen, F. Wuerthner, Z. Bao, Adv. Funct. Mater. 20 (2010) 2148–2156.
[12] H. Iino, J.-I. Hanna, Adv. Mater. 23 (2011) 1748–1751.
[13] H.S. Tan, N. Mathews, T. Cahyadi, F.R. Zhu, S.G. Mhaisalkar, Appl. Phys. Lett. 94 (2009) 263303.
[14] J.H. Oh, W.-Y. Lee, T. Noe, W.-C. Chen, M. Koenemann, Z. Bao, J. Am. Chem. Soc. 133 (2011) 4204–4207.
[15] A. Operamolla, G.M. Farinola, Eur. J. Org. Chem. 2011 (2011) 423–450.
[16] M.-H. Yoon, C. Kim, A. Facchetti, T.J. Marks, J. Am. Chem. Soc. 128 (2006) 12851–12869.
[17] B.A. Jones, A. Facchetti, M.R. Wasielewski, T.J. Marks, J. Am. Chem. Soc. 129 (2007) 15259–15278.
[18] C.A. Di, G. Yu, Y.Q. Liu, Y.L. Guo, X.N. Sun, J. Zheng, Y.G. Wen, Y. Wang, W.P. Wu, D.B. Zhu, Phys. Chem. Chem. Phys. 11 (2009) 7268–7273.
[19] A. Zen, A. Bilge, F. Galbrecht, R. Alle, K. Meerholz, J. Grenzer, D. Neher, U. Scherf, T. Farrell, J. Am. Chem. Soc. 128 (2006) 3914–3915.
[20] J.-H. Tsai, W.-Y. Lee, W.-C. Chen, C.-Y. Yu, G.-W. Hwang, C. Ting, Chem. Mater. 22 (2010) 3290–3299.
[21] X.B. Sun, Y.Q. Liu, S.Y. Chen, W.F. Qiu, G. Yu, Y.Q. Ma, T. Qi, H.J. Zhang, X.J. Xu, D.B. Zhu, Adv. Funct. Mater. 16 (2006) 917–925.
[22] X.B. Sun, Y.H. Zhou, W.C. Wu, Y.Q. Liu, W.J. Tian, G. Yu, W.F. Qiu, S.Y. Chen, D.B. Zhu, J. Phys. Chem. B 110 (2006) 7702–7707.
[23] H. Shang, H. Fan, Y. Liu, W. Hu, Y. Li, X. Zhan, J. Mater. Chem. 21 (2011) 9667–9673.
[24] A.L. Kanibolotsky, I.F. Perepichka, P.J. Skabara, Chem. Soc. Rev. 39 (2010) 2695–2728.
[25] G. Li, V. Shrotriya, J.S. Huang, Y. Yao, T. Moriarty, K. Emery, Y. Yang, Nat. Mater. 4 (2005) 864–868.
[26] Y.-C. Lai, T. Higashihara, J.-C. Hsu, M. Ueda, W.-C. Chen, Sol. Energy Mater. Sol. Cells 97 (2012) 164–170.
[27] B.C. Thompson, J.M.J. Frechet, Angew. Chem. Int. Ed. 47 (2008) 58–77.
[28] S.H. Park, A. Roy, S. Beaupre, S. Cho, N. Coates, J.S. Moon, D. Moses, M. Leclerc, K. Lee, A.J. Heeger, Nat. Photonics 3 (2009) 297–302.
[29] C. Lu, H.C. Wu, Y.C. Chiu, W.Y. Lee, W.C. Chen, Macromolecules 45 (2012) 3047–3056.
[30] C.-Y. Yu, B.-T. Ko, C. Ting, C.-P. Chen, Sol. Energy Mater. Sol. Cells 93 (2009) 613–620.
[31] Q.-D. Ling, D.-J. Liaw, C. Zhu, D.S.-H. Chan, E.-T. Kang, K.-G. Neoh, Prog. Polym. Sci. 33 (2008) 917–978.
[32] H.-C. Wu, A.-D. Yu, W.-Y. Lee, C.-L. Liu, W.-C. Chen, Chem. Commun. 48 (2012) 9135–9137.
[33] Y.-H. Chou, W.-Y. Lee, W.-C. Chen, Adv. Funct. Mater. 22 (2012) 4352–4359.
[34] W.-Y. Lee, T. Kurosawa, S.-T. Lin, T. Higashihara, M. Ueda, W.-C. Chen, Chem. Mater. 23 (2011) 4487–4497.
[35] C.-L. Liu, W.-C. Chen, Polym. Chem. 2 (2011) 2169–2174.
[36] J.A. Rogers, Z. Bao, K. Baldwin, A. Dodabalapur, B. Crone, V.R. Raju, V. Kuck, H. Katz, K. Amundson, J. Ewing, P. Drzaic, Proc. Natl. Acad. Sci. U. S. A. 98 (2001) 4835–4840.
[37] C.D. Sheraw, L. Zhou, J.R. Huang, D.J. Gundlach, T.N. Jackson, M.G. .Kane, I.G. Hill, M.S. Hammond, J. Campi, B.K. Greening, J. Francl, J. West, Appl. Phys. Lett. 80 (2002) 1088–1090.
[38] G.H. Gelinck, H.E.A. Huitema, E. Van Veenendaal, E. Cantatore, L. Schrijnemakers, J. Van der Putten, T.C.T. Geuns, M. Beenhakkers, J.B. Giesbers, B.H. Huisman, E.J. Meijer, E.M. Benito, F.J. Touwslager, A.W. Marsman, B.J.E. Van Rens, D.M. De Leeuw, Nat. Mater. 3 (2004) 106–110.
[39] B. Crone, A. Dodabalapur, Y.Y. Lin, R.W. Filas, Z. Bao, A. LaDuca, R. Sarpeshkar, H.E. Katz, W. Li, Nature 403 (2000) 521–523.
[40] J. Sun, B. Zhang, H.E. Katz, Adv. Funct. Mater. 21 (2011) 29–45.
[41] H.E. Katz, Electroanalysis 16 (2004) 1837–1842.

[42] M.E. Roberts, S.C.B. Mannsfeld, N. Queralto, C. Reese, J. Locklin, W. Knoll, Z. Bao, Proc. Natl. Acad. Sci. U. S. A. 105 (2008) 12134–12139.
[43] A.N. Sokolov, M.E. Roberts, O.B. Johnson, Y. Cao, Z. Bao, Adv. Mater. 22 (2010) 2349–2353.
[44] T.M. Pappenfus, K.R. Mann, Org. Lett. 4 (2002) 3043–3046.
[45] A. Di Carlo, F. Piacenza, A. Bolognesi, B. Stadlober, H. Maresch, Appl. Phys. Lett. 86 (2005) 263501.
[46] U.S. Jeng, C.H. Su, C.-J. Su, K.-F. Liao, W.-T. Chuang, Y.-H. Lai, J.-W. Chang, Y.-J. Chen, Y.-S. Huang, M.-T. Lee, K.-L. Yu, J.-M. Lin, D.-G. Liu, C.-F. Chang, C.-Y. Liu, C.-H. Chang, K.S. Liang, J. Appl. Crystallogr. 43 (2010) 110–121.
[47] G. Horowitz, M.E. Hajlaoui, Synth. Met. 122 (2001) 185–189.
[48] A.C. Durr, F. Schreiber, M. Munch, N. Karl, B. Krause, V. Kruppa, H. Dosch, Appl. Phys. Lett. 81 (2002) 2276–2278.
[49] Z. Bao, J. Locklin, Organic Field-Effect Transistors, CRC Press, Boca Raton, FL, 2007.
[50] S.H. Jin, A.E. Islam, T.-I. Kim, J.-H. Kim, M.A. Alam, J.A. Rogers, Adv. Funct. Mater. 22 (2012) 2276–2284.
[51] M. Shtein, J. Mapel, J.B. Benziger, S.R. Forrest, Appl. Phys. Lett. 81 (2002) 268–270.
[52] J. Lee, K. Kim, J.H. Kim, S. Im, D.Y. Jung, Appl. Phys. Lett. 82 (2003) 4169–4171.
[53] F.-C. Chen, C.-H. Liao, Appl. Phys. Lett. 93 (2008) 103310.
[54] D. Kumaki, T. Umeda, S. Tokito, Appl. Phys. Lett. 92 (2008) 093309.
[55] Y. Cui, Q.Q. Wei, H.K. Park, C.M. Lieber, Science 293 (2001) 1289–1292.
[56] E. Stern, J.F. Klemic, D.A. Routenberg, P.N. Wyrembak, D.B. Turner-Evans, A.D. Hamilton, D.A. LaVan, T.M. Fahmy, M.A. Reed, Nature 445 (2007) 519–522.